A Cystine Knot Peptide Targeting Integrin $\alpha_v\beta_6$ for Photoacoustic and Fluorescence Imaging of Tumors in Living Subjects

Chao Zhang[1,2], Richard Kimura[1], Lotfi Abou-Elkacem[1], Jelena Levi[1], Lingyun Xu[1], and Sanjiv Sam Gambhir[1]

[1]*Department of Radiology, Molecular Imaging Program at Stanford, Canary Center for Cancer Early Detection, Stanford University, Stanford, California; and* [2]*Department of Medical Ultrasound, Tongji Hospital, Tongji Medical College, Huazhong University of Science and Technology, Wuhan, China*

Photoacoustic imaging is a nonionizing biomedical imaging modality with higher resolution and imaging depth than fluorescence imaging, which has greater sensitivity. The combination of the 2 imaging modalities could improve the detection of cancer. Integrin $\alpha_v\beta_6$ is a cell surface marker overexpressed in many different cancers. Here, we report the development and evaluation of a dye-labeled cystine knot peptide, which selectively recognizes integrin $\alpha_v\beta_6$ with high affinity, for photoacoustic and fluorescence imaging. The new dual-modality probe may find clinical application in cancer diagnosis and intraoperative imaging of integrin $\alpha_v\beta_6$–positive tumors. **Methods:** An engineered cystine knot peptide, $R_0$1, that recognizes integrin $\alpha_v\beta_6$ was labeled with Atto 740 (A740) and evaluated for its specific cell uptake and its sensitivity threshold. A740-$R_0$1 was injected via the tail vein into nude mice xenografted with A431 (integrin $\alpha_v\beta_6$–positive) or 293T (integrin $\alpha_v\beta_6$–negative) tumors. Photoacoustic and fluorescence scans of tumors were acquired before and at 0.5, 1, 2, and 4 h after injection of A740-$R_0$1. Dynamic photoacoustic scans of various normal organs were also acquired. Ex vivo fluorescence imaging of tissues was performed 1 h after injection. **Results:** The A740-$R_0$1 demonstrated integrin $\alpha_v\beta_6$–dependent binding to A431 cells in culture. Sensitivity studies indicated that the probe may potentially detect lesions as small as 1 or 6 mm^3 by fluorescence or photoacoustic imaging, respectively. The photoacoustic and fluorescence signals of A431 xenografts at 1 h after injection were 1.87 ± 0.25 arbitrary units (AU) and 8.27 ± 0.87 AU, respectively. Target specificity was confirmed by low tumor uptake in 293T tumors at 1 h after injection (1.07 ± 0.15 AU and 1.10 ± 0.14 AU for photoacoustic and fluorescence signals, respectively). A740-$R_0$1 exhibited hepatobiliary clearance marked by high uptake in the liver, spleen, and intestine but low uptake in the kidneys. **Conclusion:** A740-$R_0$1 specifically targeted integrin $\alpha_v\beta_6$ with low nanomolar affinity. A740-$R_0$1 was able to detect integrin $\alpha_v\beta_6$ both in vitro and in vivo by photoacoustic and fluorescence imaging. A740-$R_0$1 is able to detect $\alpha_v\beta_6$-positive tumors in living subjects and may have clinical application in cancer diagnosis and real-time image-guided surgery.

Key Words: photoacoustic fluorescence imaging; integrin $\alpha_v\beta_6$; cystine knot

J Nucl Med 2016; 57:1629–1634
DOI: 10.2967/jnumed.115.169383

Photoacoustic imaging is a noninvasive and nonionizing biomedical imaging modality with high optical contrast and scalable ultrasound resolution and imaging depth (*1*). On the basis of the photoacoustic effect, photoacoustic imaging detects thermoelastically induced ultrasonic waves formed as a result of light absorption by molecules (*2*). Various endogenous and exogenous absorbers can serve as photoacoustic contrast agents (*3*). Primary endogenous absorbers such as hemoglobin (*4*), melanin (*5*), DNA/RNA (*6*), and lipids (*7*) may provide functional and anatomic information. Exogenous contrast agents including organic dyes (*8*), nanoparticles (*1,9*), and reporter genes (*5*) can greatly enhance photoacoustic signals and extend the applications of photoacoustic imaging to molecular imaging.

The advantages of using small-molecule fluorescent dyes (<2 nm) for in vivo imaging are their biocompatibility and rapid but complete clearance from the body (*10,11*). Fluorescent dyes may also be used in photoacoustic imaging applications. Fluorescence imaging depends on the photons emitted from the tracer, whereas photoacoustic imaging depends on photon energy absorbed but released instead as heat. Therefore, some of the physical properties that determine whether a fluorescent dye may be used in this dual application as photoacoustic agents are a high extinction coefficient but low fluorescence quantum yield (*12*). In this study, we selected a relatively photostable fluorescent dye, Atto 740 (A740), to serve as a multimodal fluorescence and photoacoustic contrast agent. A740 emits in the near-infrared region for optimal in vivo fluorescence imaging. A previous study (*13*) had shown A740 to also provide photoacoustic contrast.

Integrin $\alpha_v\beta_6$ is a transmembrane cell surface marker overexpressed in pancreatic (*14*), lung (*15*), gastric (*16*), ovarian (*17*), endometrial (*18*), colorectal (*19*), oral (*20*), and skin (*21*) cancer as well as in cholangiocarcinoma (*22*). Importantly, integrin $\alpha_v\beta_6$ is not expressed on most normal adult tissues (*23*). Thus, a molecular probe that recognizes integrin $\alpha_v\beta_6$ may be used to diagnose or treat these cancers. In a previous study, we engineered cystine knot peptides to bind integrin $\alpha_v\beta_6$ with equilibrium dissociation constants

Received Nov. 10, 2015; revision accepted Apr. 14, 2016.
For correspondence or reprints contact: Sanjiv Sam Gambhir, Molecular Imaging Program at Stanford, James H. Clark Center, 318 Campus Dr., Stanford, CA 94305-5427.
E-mail: sgambhir@stanford.edu
Published online May 26, 2016.

(K_D) of 3–6 nM (*24*). The peptides were labeled with ^{64}Cu-DOTA (*24*) and ^{18}F-fluorobenzoyl (*25*) for PET imaging. They exhibited higher accumulations in integrin $\alpha_v\beta_6$–positive xenografts (~5 and 2 percentage injected dose per gram [%ID/g], respectively) than in integrin $\alpha_v\beta_6$–negative controls (~1.3 %ID/g). Similar results (~2 %ID/g for integrin $\alpha_v\beta_6$–positive xenografts) were observed in ^{99m}Tc-based (*26*) SPECT imaging.

In contrast to PET and SPECT imaging, photoacoustic and fluorescence imaging are radiation free and have higher spatial resolution (*27,28*). However, appropriately labeled cystine knot probes for hybrid photoacoustic–fluorescence imaging of integrin $\alpha_v\beta_6$ have not yet been reported. Here, we report the design and evaluation of a probe targeting integrin $\alpha_v\beta_6$–positive tumors for dual photoacoustic and fluorescence imaging.

MATERIALS AND METHODS

Synthesis of A740-$R_0$1

A cystine knot peptide, $R_0$1, that binds integrin $\alpha_v\beta_6$ (K_D = 3.6 nM) was chemically synthesized, folded, and purified as previously described (*24*). The N terminus amine of $R_0$1 was used for site-specific attachment of A740. For labeling, both $R_0$1 and A740 *N*-hydroxysuccinimide ester (ATTO-Tec) were dissolved in anhydrous dimethylformamide (Sigma Aldrich) to afford 10 mg/mL solutions. The 2 were mixed in a 1:5 molar ratio. An equal volume of 200 mM, pH 8.3, sodium bicarbonate was added to the mixture, which reacted for up to 1 h at room temperature. A740-$R_0$1 was purified by reversed-phase high-performance liquid chromatography (Higgins Analytic). The mobile phase was 0.1% trifluoroacetic acid (Thermo Fisher Scientific) in water (solution A) and 0.1% trifluoroacetic acid in 90% acetonitrile (Thermo Fisher Scientific) in water (solution B). Purified A740-$R_0$1 was characterized by matrix-assisted laser desorption/ionization time-of-flight mass spectrometry on an AB Sciex 5800 TOF/TOF System. Lyophilized A740-$R_0$1 was resuspended in dimethyl sulfoxide (Thermo Fisher Scientific) and diluted with Dulbecco phosphate-buffered saline (DPBS) to a final concentration of 6×10^{-5} M. The maximum absorption wavelength of A740-$R_0$1 was determined by UV-Vis spectrophotometry on a Nanodrop 2000 (Thermo Fisher Scientific).

Photobleaching Study

Fifty microliters of A740-$R_0$1 (1×10^{-5} M) were analyzed with the Nexus 128 photoacoustic instrument (Endra) and scanned with laser light using the maximum absorption wavelength (750 nm) for 30 min. Photobleaching was determined by the change in photoacoustic intensity over time.

Cell Uptake Study

The human epidermoid carcinoma cell line A431 (integrin $\alpha_v\beta_6$–positive) and the human embryonic kidney 239T (integrin $\alpha_v\beta_6$–negative) (*24*) were obtained from frozen lab stocks and grown in Dulbecco modified Eagle medium supplemented with 10% fetal bovine serum and penicillin–streptomycin (Invitrogen). Cells were plated at 1×10^4 cells/cm^2 in the Petri dishes (100 mm; Corning) and grown to approximately 85% confluence. A740-$R_0$1 was added at concentrations of 0.2, 0.5, or 1 μM and incubated at 37°C for 0.5, 1, or 4 h. After cells were washed with DPBS 3 times, fluorescence microscopic images were collected on an Axiovert 200 M microscope (Zeiss). A740-$R_0$1 was excited with a 740 nm laser, and its emission was detected by a photomultiplier using a 760-nm band-pass filter. The cells were detached with trypsin (Invitrogen) and centrifuged. The harvested cell pellets were resuspended in 100 μL of DPBS and counted by hemocytometry. One million cells were pipetted into Eppendorf tubes for photoacoustic and fluorescence imaging. The cellular uptake of A740-$R_0$1 was quantified by measuring the photoacoustic and fluorescence intensity of each sample with the Nexus 128 system and the IVIS200 system (Caliper Life Sciences), respectively. A 3-dimensional (3D) region of interest was drawn over the tube for quantitative analysis of the photoacoustic signal using the software (amide.sourceforge.net) (*29*).

For the blocking study, a 10-fold molar excess of unlabeled $R_0$1 was added to final concentration of 5 μM, 10 min before addition of A740-$R_0$1.

Sensitivity Study

A431 cells were plated at 1×10^4 cells/cm^2 in the Petri dishes (100 mm) and grown to approximately 85% confluence. The cells were incubated with 0.5 μM A740-$R_0$1 for 1 h at 37°C. The cells were washed 3 times with DPBS to remove unbound A740-$R_0$1. Cells were detached with trypsin (Invitrogen) and centrifuged. The harvested cell pellets were resuspended in 100 μL of DPBS and counted by hemocytometry. The cells were serially diluted to 1.2, 0.6, 0.3, and 0.1 million in DPBS for photoacoustic and fluorescence imaging.

Small-Animal Imaging and Tissue Biodistribution

All animal experiments were performed in accordance with the regulations for the care and use of research animals approved by the Stanford University Institutional Animal Care and Use Committee. Eight-week-old female nude mice (Charles River) were injected with 2 million A431 or 5 million 293T cells (in 100 μL of DPBS) in the front leg flank. Mice (n = 3 for A431, n = 3 for 293T) bearing 0.5- to 1.0-cm xenografted tumor mass were scanned using a Nexus 128 photoacoustic imaging system. A 750-nm laser light with 240 views and 1 pulse per view was used for scanning. Data were obtained before and 0.5, 1, 2, and 4 h after administration of 200 μL of A740-$R_0$1 (6×10^{-5} M) via tail vein injection. Maximum-intensity-projection 3D photoacoustic images were reconstructed and analyzed using Osirix software (Apple). Xenograft tumors were arranged in the dimple of the animal tray to minimize any breathing and other motion artifacts. The blood vessels of the tumor on the 3D reconstructed images were selected for spatial coregistration. Mice were placed on the animal tray of the photoacoustic instrument either supine or prone for scanning of the liver, intestine, and kidneys. The mice were imaged using an optical and x-ray small-animal imaging system (Bruker) for fluorescence imaging.

Ex Vivo Studies

Mice were sacrificed 1 h after injection of 200 μL of A740-$R_0$1 (6×10^{-5} M) (n = 3). Optical imaging of excised organs was performed with the IVIS200. Quantitative analysis was performed using Living Image 4.0 software.

Statistical Analysis

Analyses were performed in SPSS 13.0 (Lead Technologies). All data were presented as the mean ± SD. Means were compared using independent-samples t test. A P value of less than 0.05 was considered statistically significant.

RESULTS

Synthesis of A740-$R_0$1

Atto 740 *N*-hydroxysuccinimide ester was used to label the cystine knot peptide $R_0$1 (Fig. 1). A740-$R_0$1 was separated from the reaction mixture by reversed-phase high-performance liquid chromatography, with a retention time of 21.5 min (Supplemental Fig. 1; supplemental materials are available at http://jnm.snmjournals.org) and verified by matrix-assisted laser desorption/ionization time-of-flight mass spectrometry with m/z of 4357 (Supplemental Fig. 2). The maximum absorption wavelength

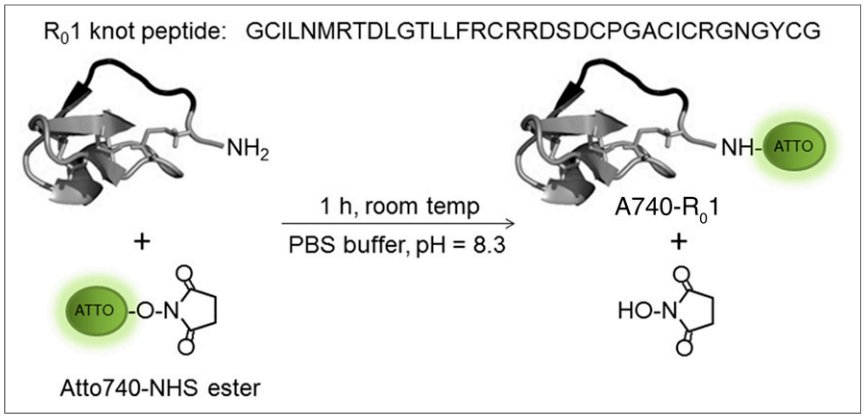

FIGURE 1. $R_0$1 contains a single primary amine located at its N terminus. This amine was used to couple A740-NHS at pH 8.3 in 200 mM sodium bicarbonate at room temperature for 1 h. A740-$R_0$1 was purified by reversed-phase high-performance liquid chromatography. NHS = *N*-hydroxysuccinimide.

of A740-$R_0$1 agent was 750 nm (Supplemental Fig. 3). The half maximal inhibitory concentration of $R_0$1 and A740-$R_0$1 was 5.9 ± 1.1 and 39.4 ± 6.5 nM, respectively (Supplemental Fig. 4).

Photobleaching Study

A740-$R_0$1 demonstrated high stability without significant decrease of photoacoustic signal after irradiation with 750-nm laser light for 30 min. Photoacoustic signals increased linearly with an increase in A740-$R_0$1 concentrations (R^2 = 0.997) (Fig. 2).

Cell Uptake Study

The binding of A740-$R_0$1 was assayed in integrin $\alpha_v\beta_6$–positive A431 and integrin $\alpha_v\beta_6$–negative 293T cells. Cell uptake of A740-$R_0$1 was clearly seen in A431 cells by fluorescence microscopy (Supplemental Fig. 5). There were significant differences in photoacoustic (Supplemental Figs. 6A and 6C) and fluorescence (Supplemental Figs. 6B and 6D) signals between A431 cells and 293T cells at different incubation times and with various concentrations of A740-$R_0$1 ($P < 0.01$). When incubated with different concentrations of A740-$R_0$1 for 1 h, the fluorescence of A431 cells remained unchanged, whereas background signals associated with 293T cells slightly increased in a dose-dependent manner. The uptake of A740-$R_0$1 after incubation for various times in both cell lines increased in a time-dependent manner (Supplemental Fig. 6). At the 1-h time point using 0.5 μM A740-$R_0$1, the photoacoustic and fluorescence signals from A431 cells were about 3- and 2.4-fold higher than that from 293T cells, respectively. Blocking of $\alpha_v\beta_6$ integrin receptors with a 10-fold molar excess of unlabeled $R_0$1 peptide resulted in a significantly ($P < 0.01$) decreased cellular uptake of A740-$R_0$1 (about 64% and 47% decrease of photoacoustic and fluorescence signals, respectively). These results confirm the specific high-affinity binding of A740-$R_0$1 to integrin $\alpha_v\beta_6$–expressing cells (Fig. 3).

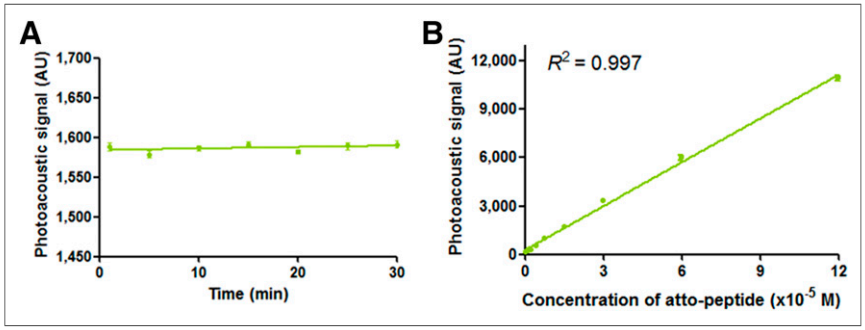

FIGURE 2. Photobleaching study. (A) Photoacoustic signal of A740-$R_0$1 was stable on exposure to 750-nm laser light for 30 min. (B) Photoacoustic signal was linearly dependent on concentration of A740-$R_0$1 (R^2 = 0.997).

Sensitivity Study

The minimum detectable number of A431 cells labeled with A740-$R_0$1 was determined to be 0.1 million using fluorescence imaging (P = 0.03 when compared with blank) and 0.6 million with photoacoustic imaging (P = 0.001 when compared with blank) (Fig. 4).

Small-Animal Imaging and Tissue Biodistribution

The efficacy of A740-$R_0$1 to detect $\alpha_v\beta_6$ in vivo was studied in xenografts implanted in nude mice (Fig. 5A; Supplemental Fig. 7; Supplemental Video 1). Higher photoacoustic and fluorescence signals were observed at all times after injection (0.5, 1, 2, and and 4 h) in mice with A431 xenografts than in 293T xenografts ($P < 0.05$) (Fig. 5B). In vivo photoacoustic imaging of A431 xenografts showed a 2-fold-higher signal (1.87 ± 0.25 arbitrary units [AU]) than the baseline (0.99 ± 0.10 AU) and significantly higher signals (P = 0.005) than 293T xenografts after administration of A740-$R_0$1. However, the photoacoustic signal of 293T xenografts before (0.96 ± 0.05 AU) and 1 h after (1.07 ± 0.15 AU) administration of A740-$R_0$1 showed no significant (P = 0.317) photoacoustic signal increase (Fig. 5). The fluorescence signal of A431 xenografts at 1 h after injection was 8.27 ± 0.87 AU, an 8-fold increase over the value of 1.01 ± 0.07 AU before injection of A740-$R_0$1 (P = 0.005). The fluorescence signal of 293T xenografts at 1 h after injection was 1.10 ± 0.14 AU, which was approximately the same as the preinjection value of 1.00 ± 0.02 AU (P = 0.424) (Fig. 5).

The biodistribution of A740-$R_0$1 in the liver, intestine, and kidneys was detected in vivo by photoacoustic imaging. An increased signal in the liver was observed 1 h after injection of A740-$R_0$1. Temporally dependent increases in photoacoustic signals were detected in the intestines, reaching peak value at 4 h after injection. Minimal photoacoustic contrast was observed for the kidneys throughout the study (Supplemental Fig. 8). Comparatively, the biodistribution of A740-$R_0$1 in various organs was also determined ex vivo by fluorescence imaging (Fig. 6A). The highest maximum radiance was observed in the liver, followed by the intestines, spleen, and kidneys (Fig. 6B).

DISCUSSION

The endogenous optical absorber hemoglobin enables photoacoustic imaging of

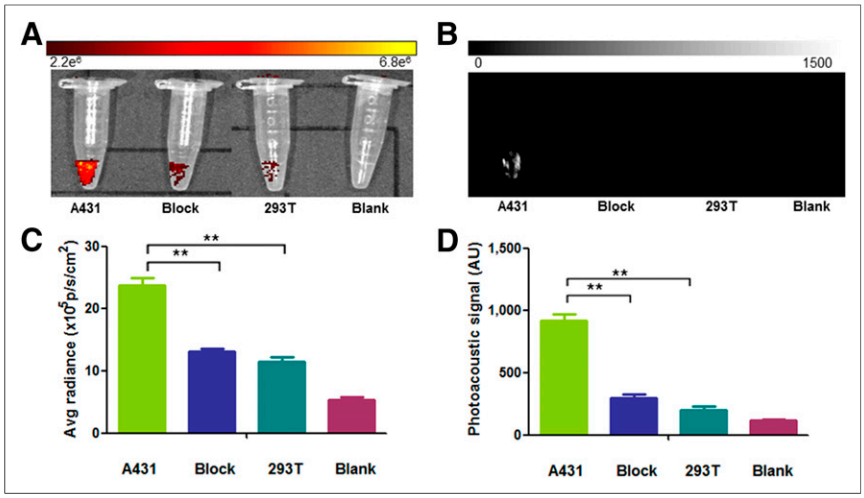

FIGURE 3. Cell uptake study. Fluorescence (A) and photoacoustic (B) imaging of cells in Eppendorf tubes labeled with A740-$R_0$1 with or without a 10-fold excess of unlabeled $R_0$1 peptide (Block). Higher fluorescence and photoacoutic signal could be detected in A431 cells ($\alpha_v\beta_6$-positive) compared with 293T cells ($\alpha_v\beta_6$-negative) and block groups. (C and D) Quantitative analysis of fluorescence and photoacoustic signals. Data are shown as mean ± SD (n = 3). $^{**}P < 0.001$. Avg = average.

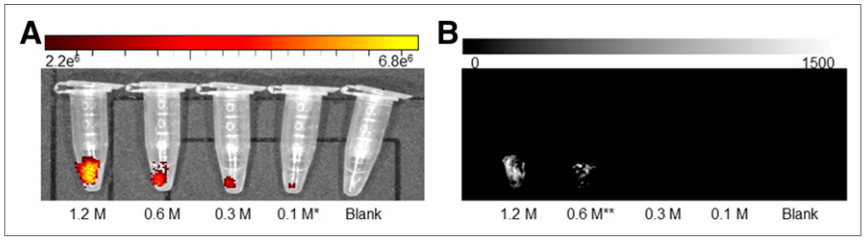

FIGURE 4. Sensitivity study. Fluorescence (A) and photoacoustic (B) imaging of various numbers of A431 cells labeled with A740-$R_0$1. Quantitative analysis showed lowest detectable number of labeled A431 cells to be 0.1 million for fluorescence imaging and 0.6 million for photoacoustic imaging.

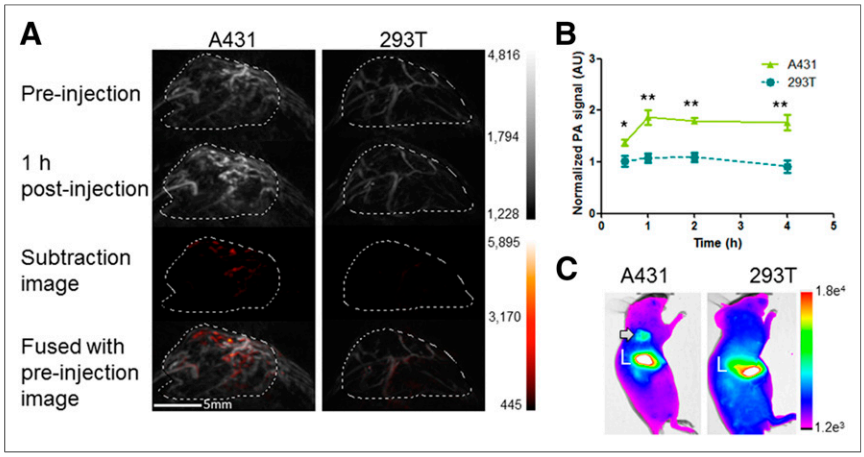

FIGURE 5. Imaging of tumors. (A) Photoacoustic imaging of tumors. Microvascular structures could be observed in both A431 and 293T xenografts. Clear enhancement of photoacoustic signal could be seen in A431 xenografts 1 h after tail vein injection of A740-$R_0$1, whereas there was only minor change in 293T xenografts. (B) Higher photoacoustic signals were detected at all time points in A431 xenografts than 293T xenografts. Maximum enhancement could be seen at 1 h after injection of A740-$R_0$1. $^{*}P < 0.05$. $^{**}P < 0.01$. (C) Fluorescence imaging of xenografts 1 h after injection of A740-$R_0$1. A431 xenograft (arrow) was clearly visible relative to background. L = liver.

the blood vasculature. Some cancers, such as breast cancer, may be detected without the need for exogenous contrast agents because of differential contrast between hemoglobin-rich tumors and hemoglobin-deprived fat and glandular tissues (*4*). In this study, we obtained 3D photoacoustic images of the blood vasculature using 750-nm light (Fig. 5A). However, information about the blood vasculature is often not enough to confirm the diagnosis.

Exogenous agents provide the means to elucidate molecular information, which can be used together with anatomic imaging data to produce a more accurate diagnosis. Exogenous agents can be composed of complementary components that perform dedicated functions such as tumor targeting and photoacoustic contrast. To develop photoacoustic imaging agents for cancer detection in humans, the long-term safety profiles of several metallic photoacoustic contrast agents are presently being evaluated for toxicity (*30*). At the same time, cystine knot peptides that recognize integrin $\alpha_v\beta_6$ are being evaluated in humans as PET agents for pancreatic cancer. In this study, we coupled a cystine knot peptide to a biocompatible organic dye, A740-$R_0$1, and evaluated it as a multimodal photoacoustic–fluorescence imaging agent for cancer detection in living subjects.

The cystine knot peptide, $R_0$1, was labeled with Atto 740 through the peptide's sole amine located at its N terminus. A740-$R_0$1 demonstrated high uptake in integrin $\alpha_v\beta_6$–positive cells. The probe sensitivity was sufficiently high enough to detect as few as 0.6 million cells by photoacoustic imaging. In vivo studies of A740-$R_0$1 also show that integrin $\alpha_v\beta_6$–positive xenografts had a 2-fold-greater photoacoustic signal than integrin $\alpha_v\beta_6$–negative controls 1 h after tail vein injection (Fig. 5B). The photoacoustic signals do not change significantly from 1 to 4 h after injection (Supplemental Fig. 7), a phenomenon observed in previous studies with knottin peptides labeled with Cy5.5 (*31*). Much of the peptide clears the blood pool relatively quickly, so that any signal enhancement at the tumor represents either probe that is bound to the targeted receptor or probe that has been internalized by tumor cells. Importantly, these new imaging capabilities provide an additional level of molecular information for diagnosis and prognosis of disease marked by integrin $\alpha_v\beta_6$ overexpression (*25*).

A740-$R_0$1 can also simultaneously be used for fluorescence imaging of tumors in living subjects. In this study, 0.1 million cells in 100 μL DPBS can be detected by fluorescence imaging. There are approximately

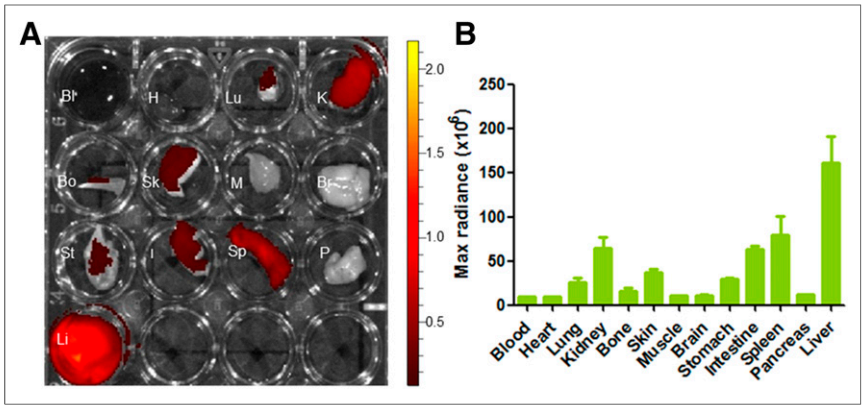

FIGURE 6. Biodistribution of A740-$R_0$1. (A) Ex vivo fluorescence imaging of various organs 1 h after tail vein injection of A740-$R_0$1. (B) Quantitative analysis showed highest maximum radiance was observed in liver, followed by intestine, spleen, and kidneys. Bl = blood; Bo = bone; Br = brain; H = heart; I = intestine; K = kidney; Li = liver; Lu = lung; M = muscle; max = maximum; P = pancreas; Sk = skin; Sp = spleen; St = stomach.

10 million cells in a 100 mm^3 tumor (*13*), so that A740-$R_0$1 could potentially detect lesions as small as 1 mm^3 by fluorescence imaging. These hypotheses bode well for early detection of cancer.

We observed a difference in contrast enhancement between integrin $\alpha_v\beta_6$–positive and integrin $\alpha_v\beta_6$–negative tumors using both fluorescence and photoacoustic imaging. Fluorescence imaging can record 8-fold difference between positive and negative tumors 1 h after injection. In contrast, photoacoustic imaging showed a modest approximately 2-fold change. This phenomenon is consistent with the research by Xu et al. (*32*). This difference may be attributed to the difference in the efficiency of energy transfer through living tissue via different modalities.

Although fluorescence imaging has greater sensitivity at these depths, photoacoustic imaging has better spatial resolution. Therefore, bridging the 2 imaging modalities may improve detection of cancer in several ways. The photoacoustic properties of multifunctional probes have the potential to provide surgeons with a 3D image of a tumor located deep within tissues. Because photoacoustic imaging systems use an ultrasonic transducer to process signals, photoacoustic capabilities can be incorporated into standard ultrasound instruments. Moreover, real-time photoacoustic images can be obtained if the pulse repetition rate of the laser source is sufficiently fast (*33*). At the same time, the probe's fluorescence should enhance detection of residual diseases in the surgical cavity (*34*). In this study, the cell-sensitivity assay as well as the in vivo and ex vivo imaging data show that the probe's fluorescence signal can be detected in a highly sensitive manner. These multimodal approaches should provide additional real-time clinical information to improve surgical accuracy and ultimately treatment outcome (*35*).

In previous studies, high off-target kidney uptake was observed when cystine knot peptides were labeled with ^{64}Cu-DOTA (*24*), ^{18}F-fluorobenzoate (*25*), and ^{99m}Tc-single amino acid chelate (*26*) for PET and SPECT imaging. The ex vivo data from this study showed that the hydrophobic A740 dye strongly influenced the pharmacokinetics and tissue biodistribution of the probe. A740-$R_0$1 exhibited extremely high uptake in the liver, spleen, and intestines, indicating excretion of the probe through the hepatobiliary rather than urinary system. Interestingly, this study suggests that colabeling peptide-based tracers with organic dyes may be a way to decrease renal retention of radiotracers because off-target uptake may be shared by 2 clearance systems so that toxicity to any one organ system may be reduced.

There are some issues that need to be addressed in future studies. The enhanced photoacoustic signal is only about 2-fold higher than the preinjection signal, which is relatively lower than the signal enhancement gained from metallic nanoparticles (*9*). We may try to increase the labeling ratio of the probe to increase photoacoustic signal by evaluating larger-affinity ligands such as antibody fragments, which may be endowed with more favorable pharmacokinetics. In addition, other organic dyes or quenchers may be better photoacoustic contrast agents. These hypotheses are currently under study.

CONCLUSION

To our knowledge, this is the first report of molecular photoacoustic imaging for detection of integrin $\alpha_v\beta_6$–positive xenografts in living animals. The A740-labeled cystine knot peptide probe A740-$R_0$1 enabled imaging of integrin $\alpha_v\beta_6$–positive tumors by both photoacoustic and fluorescence imaging. Tumor uptake was rapid and high. Clearance of the probe also occurred quickly through the hepatobiliary system, so that renal uptake was low. On further development and validation, these types of probes may find clinical application in cancer diagnosis as well as in intraoperative imaging.

DISCLOSURE

The costs of publication of this article were defrayed in part by the payment of page charges. Therefore, and solely to indicate this fact, this article is hereby marked "advertisement" in accordance with 18 USC section 1734. This work was supported in part by NCI ICMIC P50CA114747 (SSG), The Canary Foundation, the Ben & Catherine Ivy Foundation, and the Sir Peter Michael Foundation. No other potential conflict of interest relevant to this article was reported.

REFERENCES

1. Kircher MF, de la Zerda A, Jokerst JV, et al. A brain tumor molecular imaging strategy using a new triple-modality MRI-photoacoustic-Raman nanoparticle. *Nat Med.* 2012;18:829–834.
2. Beard P. Biomedical photoacoustic imaging. *Interface Focus.* 2011;1:602–631.
3. Kim C, Favazza C, Wang LV. In vivo photoacoustic tomography of chemicals: high-resolution functional and molecular optical imaging at new depths. *Chem Rev.* 2010;110:2756–2782.
4. Kruger RA, Lam RB, Reinecke DR, Del Rio SP, Doyle RP. Photoacoustic angiography of the breast. *Med Phys.* 2010;37:6096–6100.
5. Qin C, Cheng K, Chen K, et al. Tyrosinase as a multifunctional reporter gene for photoacoustic/MRI/PET triple modality molecular imaging. *Sci Rep.* 2013;3:1490.
6. Yao DK, Chen R, Maslov K, Zhou Q, Wang LV. Optimal ultraviolet wavelength for in vivo photoacoustic imaging of cell nuclei. *J Biomed Opt.* 2012;17:056004.
7. Wang B, Su JL, Amirian J, Litovsky SH, Smalling R, Emelianov S. Detection of lipid in atherosclerotic vessels using ultrasound-guided spectroscopic intravascular photoacoustic imaging. *Opt Express.* 2010;18:4889–4897.
8. Levi J, Kothapalli SR, Ma TJ, Hartman K, Khuri-Yakub BT, Gambhir SS. Design, synthesis, and imaging of an activatable photoacoustic probe. *J Am Chem Soc.* 2010;132:11264–11269.

9. de la Zerda A, Bodapati S, Teed R, et al. Family of enhanced photoacoustic imaging agents for high-sensitivity and multiplexing studies in living mice. *ACS Nano.* 2012;6:4694–4701.
10. Wang LV, Hu S. Photoacoustic tomography: in vivo imaging from organelles to organs. *Science.* 2012;335:1458–1462.
11. Kim C, Song KH, Gao F, Wang LV. Sentinel lymph nodes and lymphatic vessels: noninvasive dual-modality in vivo mapping by using indocyanine green in rats–volumetric spectroscopic photoacoustic imaging and planar fluorescence imaging. *Radiology.* 2010;255:442–450.
12. Zackrisson S, van de Ven SM, Gambhir SS. Light in and sound out: emerging translational strategies for photoacoustic imaging. *Cancer Res.* 2014;74:979–1004.
13. Levi J, Sathirachinda A, Gambhir SS. A high affinity, high stability photoacoustic agent for imaging gastrin releasing peptide receptor in prostate cancer. *Clin Cancer Res.* 2014;20:3721–3729.
14. Sipos B, Hahn D, Carceller A, et al. Immunohistochemical screening for β_6-integrin subunit expression in adenocarcinomas using a novel monoclonal antibody reveals strong up-regulation in pancreatic ductal adenocarcinomas in vivo and in vitro. *Histopathology.* 2004;45:226–236.
15. Elayadi AN, Samli KN, Prudkin L, et al. A peptide selected by biopanning identifies the integrin alphavbeta6 as a prognostic biomarker for nonsmall cell lung cancer. *Cancer Res.* 2007;67:5889–5895.
16. Zhuang Z, Zhou R, Xu X, et al. Clinical significance of integrin $\alpha_v\beta_6$ expression effects on gastric carcinoma invasiveness and progression via cancer-associated fibroblasts. *Med Oncol.* 2013;30:580.
17. Ahmed N, Pansino F, Clyde R, et al. Overexpression of $\alpha_v\beta_6$ integrin in serous epithelial ovarian cancer regulates extracellular matrix degradation via the plasminogen activation cascade. *Carcinogenesis.* 2002;23:237–244.
18. Hecht JL, Dolinski BM, Gardner HA, Violette SM, Weinreb PH. Overexpression of the $\alpha_v\beta_6$ integrin in endometrial cancer. *Appl Immunohistochem Mol Morphol.* 2008;16:543–547.
19. Yang GY, Xu KS, Pan ZQ, et al. Integrin alpha v beta 6 mediates the potential for colon cancer cells to colonize in and metastasize to the liver. *Cancer Sci.* 2008;99:879–887.
20. Xue H, Atakilit A, Zhu W, Li X, Ramos DM, Pytela R. Role of the $\alpha_v\beta_6$ integrin in human oral squamous cell carcinoma growth in vivo and in vitro. *Biochem Biophys Res Commun.* 2001;288:610–618.
21. Janes SM, Watt FM. Switch from $\alpha_v\beta_5$ to $\alpha_v\beta_6$ integrin expression protects squamous cell carcinomas from anoikis. *J Cell Biol.* 2004;166:419–431.
22. Patsenker E, Wilkens L, Banz V, et al. The $\alpha_v\beta_6$ integrin is a highly specific immunohistochemical marker for cholangiocarcinoma. *J Hepatol.* 2010;52:362–369.
23. Breuss JM, Gallo J, DeLisser HM, et al. Expression of the beta 6 integrin subunit in development, neoplasia and tissue repair suggests a role in epithelial remodeling. *J Cell Sci.* 1995;108:2241–2251.
24. Kimura RH, Teed R, Hackel BJ, et al. Pharmacokinetically stabilized cystine knot peptides that bind alpha-v-beta-6 integrin with single-digit nanomolar affinities for detection of pancreatic cancer. *Clin Cancer Res.* 2012;18:839–849.
25. Hackel BJ, Kimura RH, Miao Z, et al. ^{18}F-fluorobenzoate-labeled cystine knot peptides for PET imaging of integrin $\alpha_v\beta_6$. *J Nucl Med.* 2013;54:1101–1105.
26. Zhu X, Li J, Hong Y, et al. ^{99m}Tc-labeled cystine knot peptide targeting integrin $\alpha_v\beta_6$ for tumor SPECT imaging. *Mol Pharm.* 2014;11:1208–1217.
27. Wang LV. Multiscale photoacoustic microscopy and computed tomography. *Nat Photonics.* 2009;3:503–509.
28. Su JL, Wang B, Wilson KE, et al. Advances in clinical and biomedical applications of photoacoustic imaging. *Expert Opin Med Diagn.* 2010;4:497–510.
29. Leoning AM, Gambhir SS. AMIDE: a free software tool for multimodality medical image analysis. *Mol Imaging.* 2003;2:131–137.
30. Mehrmohammadi M, Yoon SJ, Yeager D, Emelianov SY. Photoacoustic imaging for cancer detection and staging. *Curr Mol Imaging.* 2013;2:89–105.
31. Kimura RH, Miao Z, Cheng Z, Gambhir SS, Cochran JR. A dual-labeled knottin peptide for PET and near-infrared fluorescence imaging of integrin expression in living subjects. *Bioconjug Chem.* 2010;21:436–444.
32. Xu C, Kumavor PD, Alqasemi U, et al. Indocyanine green enhanced co-registered diffuse optical tomography and photoacoustic tomography. *J Biomed Opt.* 2013;18:126006.
33. Song L, Kim C, Maslov K, Shung KK, Wang LV. High-speed dynamic 3D photoacoustic imaging of sentinel lymph node in a murine model using an ultrasound array. *Med Phys.* 2009;36:3724–3729.
34. Xi L, Zhou G, Gao N, et al. Photoacoustic and fluorescence image-guided surgery using a multifunctional targeted nanoprobe. *Ann Surg Oncol.* 2014;21:1602–1609.
35. Savage N. Technology: multiple exposure. *Nature.* 2013;502:S90–S91.